

# Material dynamics under extreme conditions of pressure and strain rate

**B. A. Remington<sup>\*1</sup>, P. Allen<sup>1</sup>, E. M. Bringa<sup>1</sup>, J. Hawreliak<sup>1</sup>, D. Ho<sup>1</sup>, K. T. Lorenz<sup>1</sup>, H. Lorenzana<sup>1</sup>, J. M. McNaney<sup>1</sup>, M. A. Meyers<sup>2</sup>, S. W. Pollaine<sup>1</sup>, K. Rosolankova<sup>3</sup>, B. Sadik<sup>1</sup>, M. S. Schneider<sup>2</sup>, D. Swift<sup>4</sup>, J. Wark<sup>3</sup> and B. Yaakobi<sup>5</sup>**

Solid state experiments at extreme pressures (10–100 GPa) and strain rates ( $10^6$ – $10^8$  s<sup>-1</sup>) are being developed on high energy laser facilities, and offer the possibility for exploring new regimes of materials science. These extreme solid state conditions can be accessed with either shock loading or with a quasi-isentropic ramped pressure drive. Velocity interferometer measurements establish the high pressure conditions. Constitutive models for solid state strength under these conditions are tested by comparing 2D continuum simulations with experiments measuring perturbation growth from the Rayleigh–Taylor instability in solid state samples. Lattice compression, phase and temperature are deduced from extended X-ray absorption fine structure (EXAFS) measurements, from which the shock induced  $\alpha$ – $\omega$  phase transition in Ti and the  $\alpha$ – $\epsilon$  phase transition in Fe, are inferred to occur on subnanosec time scales. Time resolved lattice response and phase can also be measured with dynamic X-ray diffraction measurements, where the elastic–plastic (1D–3D) lattice relaxation in shocked Cu is shown to occur promptly (<1 ns). Subsequent large scale molecular dynamics (MD) simulations elucidate the microscopic dislocation dynamics that underlies this 1D–3D lattice relaxation. Deformation mechanisms are identified by examining the residual microstructure in recovered samples. The slip-twinning threshold in single crystal Cu shocked along the [001] direction is shown to occur at shock strengths of  $\sim$ 20 GPa, whereas the corresponding transition for Cu shocked along the [134] direction occurs at higher shock strengths. This slip twinning threshold also depends on the stacking fault energy (SFE), being lower for low SFE materials. Designs have been developed for achieving much higher pressures,  $P > 1000$  GPa, in the solid state on the National Ignition Facility (NIF) laser.

**Keywords:** Material dynamics, High pressure strength, Laser experiments

## Introduction

Over the past decade, there has been a surge of activity in the field of materials science under extreme conditions of pressure  $P$ , compression ( $\rho/\rho_0$ ) and strain rate ( $d\epsilon/dt$ ), sometimes referred to as high energy density (HED) materials science. The present work is being done on HED facilities, such as high energy lasers and magnetic pinch facilities, which can create the extraordinarily high pressures in samples and have specialised diagnostics to make in situ time resolved measurements of the material properties.<sup>1–3</sup> One of the long range goals of our work in this area, aimed at the NIF laser,<sup>4</sup> is to develop the ability to experimentally test models of high pressure material

properties, such as compressibility, phase, material strength and lattice kinetics, at pressures  $P > 1000$  GPa (10 Mbar), which are essentially unexplored to date.<sup>5</sup> There are a number of challenges to overcome to achieve this goal. Achieving such high pressures ( $P \gg 1$  Mbar) in the solid state is very difficult. Extreme pressures can only be generated in small samples, 10–100  $\mu$ m thick, and can only be maintained for very brief intervals, a few tens of nanoseconds. Yet the pressures have to be applied gently enough in a ramped quasi-isentropic load so that the compression wave does not steepen into a strong shock and melt the sample. Once such extreme pressures are reached, they can only be held for an interval of  $\sim$ 10 ns, during which time strength and all the quantities that affect it, such as compression, temperature, strain rate, phase and ultimately dislocation density, need to be measured. The progress towards this challenging goal is reviewed in the present paper.

First, several standard constitutive models are reviewed for high – ( $P$ ,  $d\epsilon/dt$ ) strength. Second, the

<sup>1</sup>Lawrence Livermore National Laboratory, Livermore, CA

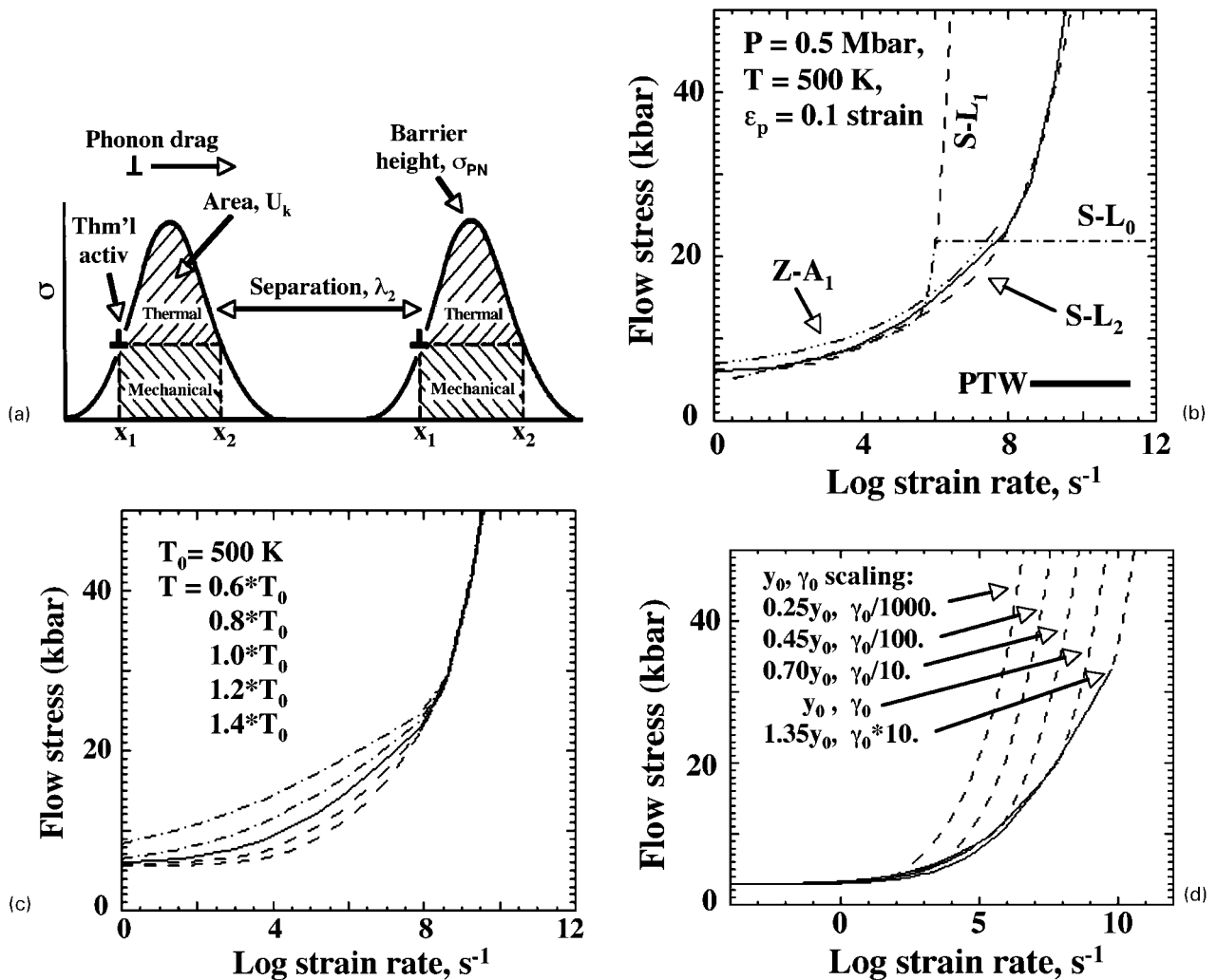
<sup>2</sup>UC San Diego, San Diego, CA

<sup>3</sup>University of Oxford, Oxford, UK

<sup>4</sup>Los Alamos National Laboratory, Los Alamos, NM

<sup>5</sup>Laboratory for Laser Energetics, University of Rochester, Rochester, NY

\*Corresponding author, email remington2@llnl.gov



a schematic of the mechanisms of deformation by stress assisted thermal activation and phonon drag; b flow stress (kbar) versus log strain rate for variety of constitutive models (see text for details) for Ta at 0.5 Mbar, temperature of 500 K and plastic strain of 0.1: nominal Steinberg-Lund model is shown by broken curve labelled S-L<sub>0</sub>; Steinberg-Lund with the artificial cap on  $\sigma_T$  removed by S-L<sub>1</sub>; Steinberg-Lund modified to resemble Preston-Tonks-Wallace (PTW) by S-L<sub>2</sub>; nominal PTW model is shown by the solid curve, and slightly refined Zerilli-Armstrong model, suitable for these high pressures and strain rates, is shown by the broken curve labelled Z-A<sub>1</sub>; c flow stress versus log strain rate for the PTW model for Ta at  $P=0.5$  Mbar,  $\epsilon_p=0.1$  strain,  $\rho/\rho_0=1.1$  compression, varying temperature by 20 and 40%; d flow stress (kbar) versus log strain rate for the PTW model for Ta at  $P=0.5$  Mbar,  $T=500$  K and  $\epsilon_p=0$ , varying parameter  $\gamma \sim \rho_m b^2$  to affect the high strain rate regime, while varying  $\gamma_0$  to hold the low strain rate regime fixed; solid curves represent athermal (lowest strain rate region) and thermal activation regimes, whereas broken curves represent the phonon drag regime<sup>3</sup>

## 1 Constitutive models

'drive', i.e. applied pressure versus time, is described. Third, the Rayleigh-Taylor instability experiments developed to test high pressure models of material strength are described. Fourth, the polycrystalline lattice diagnostic of dynamic EXAFS is discussed, followed by the single crystal lattice diagnostic of dynamic diffraction. Following that, recovery experiments and observation of the slip twinning threshold are described. Remarks about potential dynamic materials science experiments at extremely high pressures that are being designed for the NIF laser are given in the conclusions.

## Constitutive models

There is a considerable variety of constitutive models for material strength in common use, such as the Johnson-Cook,<sup>6</sup> Zerilli-Armstrong,<sup>7-9</sup> mechanical threshold stress (MTS),<sup>10</sup> thermal activation phonon

drag,<sup>11,12</sup> Steinberg-Lund,<sup>13</sup> Steinberg-Guinan<sup>14</sup> and Preston-Tonks-Wallace<sup>15</sup> models. At the high strain rates relevant to the work described in the present paper, thermal activation and dislocation glide along slip planes, resisted by phonon drag, are believed to be the dominant (rate determining) mechanisms underlying deformation,<sup>11-13,16,17</sup> as illustrated schematically in Fig. 1a.<sup>18</sup> In the thermal activation regime, dislocations are assumed to be pinned against barriers until a thermal fluctuation can kick them over the obstacle to glide to the next barrier. In this 'jerky glide' regime,<sup>12</sup> the strain rate can be written as

$$\dot{\epsilon} = \frac{\rho_m b^2}{\lambda_b \nu_a \exp\left\{\frac{F_0}{kT} \left[1 - \left(\frac{\sigma}{\tau_{MTS}}\right)^{p+q}\right]\right\} + \frac{D}{\sigma}} \quad (1)$$

Here,  $\rho_m$ ,  $b$ ,  $\lambda_b$ ,  $\nu_a$ ,  $D$  and  $\sigma$  correspond to mobile dislocation density, Burgers vector, average distance

between barriers, Debye frequency, linear photon drag coefficient and applied shear stress respectively. The  $F_0$  represents the energy required to push the dislocation over the barrier at  $T=0$  K,  $\tau_{\text{MTS}}$  corresponds to the mechanical threshold stress, which is the stress at  $T=0$  K required to surmount the peak of the barrier, and  $p$  and  $q$  represent barrier shape parameters.<sup>17</sup>

The above constitutive model assumes rigid dislocations that are undistorted in surmounting a barrier. This assumption is not appropriate for the strong Peierls barriers  $\sigma_P$  of a bcc lattice. In this case, the dislocation bows considerably in moving over a barrier, nucleating and propagating a pair of dislocation kinks.<sup>19</sup> One constitutive equation, the Hoge–Mukherjee model, which is appropriate for a bcc lattice, can be written as<sup>11</sup>

$$\dot{\varepsilon} = \frac{\rho_m b^2}{\frac{1}{\dot{\varepsilon}_0} \exp \left[ \frac{2U_k}{kT} \left( 1 - \frac{\sigma}{\sigma_P} \right)^2 \right] + \frac{D}{\sigma}} \quad (2)$$

where  $1/\dot{\varepsilon}_0 = 2w^2/(Lav)$ . Here,  $L$  is the dislocation line length,  $w$  the width of the critical pair of kinks,  $v$  the Debye frequency,  $a$  the separation between Peierls valleys, and  $2U_k$  the energy to form a pair of kinks in the dislocation segment. Note the similarity to equation (1) if  $p=1$  and  $q=2$ .

An alternate constitutive equation that explicitly includes the effects of pressure, temperature and compression, proposed for extremely high strain rates, is the Steinberg–Guinan model.<sup>14</sup> The basis for this model is the assumption that above some critical strain rate,  $\sim 10^5 \text{ s}^{-1}$ , all hardening effects owing to strain rate have saturated and the material strength becomes independent of strain rate. The only parameters that affect strength in this model are pressure, temperature compression ( $P$ ,  $T$ ,  $\eta = \rho/\rho_0$ ) and strain  $\varepsilon$ . The model is essentially a first order Taylor expansion in pressure and temperature with a work hardening prefactor  $f(\varepsilon)$  and a small correction for compression

$$\sigma = \sigma_0 f(\varepsilon) \frac{G}{G_0} \quad (3a)$$

$$\frac{G}{G_0} = 1 + \left( \frac{G'_P}{G_0} \right) \frac{P}{\eta^{1/3}} + \left( \frac{G'_T}{G_0} \right) (T - 300) \quad (3b)$$

$$f(\varepsilon) = [1 + \beta(\varepsilon_i + \varepsilon)]^n \quad (3c)$$

Where  $\sigma_0$  and  $G_0$  are the ambient strength and shear modulus,  $G'_P = \partial G / \partial P$ , and  $G'_T = \partial G / \partial T$  are the partial derivatives of shear modulus with pressure and temperature. It is assumed that the rate of change of strength with  $P$  and  $T$  is the same as that of the shear modulus  $G$ , an assumption that remains unproven under extreme conditions owing to the lack of controlled data.

The Steinberg–Lund (S–L) model<sup>13</sup> is a combination of the two models just described and is written

$$\sigma = [\sigma_T(\dot{\varepsilon}, T) + \sigma_A f(\varepsilon)] \frac{G(P, T)}{G_0} \quad (4a)$$

where the thermally activated term  $\sigma_T(\dot{\varepsilon}, T)$  is given by

$$\dot{\varepsilon} = \frac{1}{\frac{1}{C_1} \exp \left[ \frac{2U_k}{kT} \left( 1 - \frac{\sigma}{\sigma_P} \right)^2 \right] + \left( \frac{C_2}{\sigma} \right)^m} \quad (4b)$$

the  $\sigma_T(\dot{\varepsilon}, T)$  component is assumed applicable only when

$\sigma \leq \sigma_P$ , and is set to zero otherwise. Here,  $m=1$  corresponds to the standard form of the Steinberg–Lund (S–L) model; other values are discussed below. In its nominal form when  $\sigma > \sigma_P$ , the S–L model assumes that  $\sigma \approx \sigma_A f(\varepsilon) G/G_0$ , which is essentially equation (3a), the Steinberg–Guinan, strain rate independent model. Note that this construction essentially prevents phonon drag from being activated. Note also that equation (4b) is identical with the Hoge–Mukherjee model (equation (2)), provided that  $C_1 = \rho_m Lab^2 v / (2w^2) = \dot{\varepsilon}_0$ ,  $C_2 = D / (\rho_m b^2)$  and  $m=1$ . In equation (4),  $\sigma_A$ ,  $C_1$ ,  $U_k$ ,  $\sigma_P$  and  $C_2$  are all assumed to be constants, and the scaling with  $P$  and  $T$  is taken into account with the  $G/G_0$  overall factor in equation (4a). A ‘hybrid’ form of the S–L model can also be written down. When  $\sigma > \sigma_P$ , if the exponential term in the denominator of equation (4b) is set to zero and if the phonon drag term is allowed to activate, equation (4a and b) would be similar to the Hoge–Mukherjee model, only with work and pressure hardening (through scaling with the shear modulus) included.

The next model that we mention is the PTW model.<sup>15</sup> In a somewhat simplified form and for low strains, it is written here as

$$\sigma_{\text{PTW}}(\dot{\varepsilon}) = (2G) \times \max \left\{ \left[ y_0 - (y_0 - y_\infty) \text{erf} \left( \kappa T \ln \frac{\gamma \dot{\varepsilon}}{\dot{\varepsilon}} \right) \right] s_0 \left( \frac{\dot{\varepsilon}}{\gamma \dot{\varepsilon}} \right)^\beta \right\} \quad (5)$$

Where,  $y_0$ ,  $y_\infty$ ,  $\kappa$ ,  $\gamma$ ,  $s_0$  and  $\beta$  are material constants,  $\dot{\varepsilon} = c_T/2a = \omega_D/3\pi^{1/2}$  is the reference strain rate ( $c_T$  is the shear wave speed,  $a$  the interatomic spacing,  $\omega_D$  the Debye frequency), and  $G$  is the pressure and temperature dependent shear modulus. This model is based on the same mechanisms as the Hoge–Mukherjee or hybrid S–L models above, namely, thermal activation for shear stresses lower than the dominant dislocation barriers, and a viscous drag mechanism for shear stresses above the barriers. At strain rates  $d\varepsilon/dt \leq 10^4$ , the model is calibrated against Hopkinson bar and other conventional data. At strain rates  $d\varepsilon/dt > \sim 10^9 \text{ s}^{-1}$ , the model is formulated to reproduce overdriven shock data with strength assumed to be a power law of strain rate  $\sigma \sim (d\varepsilon/dt)^\beta$  ( $\beta \approx 1/4$ ). In the absence of additional data, the region in between Hopkinson bar and shock data is bridged by extrapolating the strength curves from these two regimes (thermal activation on the low end and nonlinear viscous drag on the high end) until they meet.

The last model discussed is the Zerilli–Armstrong model.<sup>7–9,20</sup> The version described for Ta<sup>8</sup> is written as

$$\sigma = c_0 + K\dot{\varepsilon}^n + B_0 e^{-\beta T} \quad (6)$$

where  $c_0 = \sigma_G + kl^{-1/2}$  and  $\beta = \beta_0 - \beta_1 \ln \dot{\varepsilon}$ . Here,  $\sigma_G$  and  $l$  correspond to the athermal stress owing to the initial defect density and grain size, and  $K$ ,  $\beta_0$ ,  $\beta_1$  and  $n$  are material constants. The form of the thermal activation term  $B_0 e^{-\beta T}$  was motivated originally by the data of Heslop and Petch for flow stress versus temperature.<sup>21,22</sup> At the strain rates where this model has been traditionally applied,  $\beta = \beta_0 - \beta_1 \ln \dot{\varepsilon} > 0$ , so that automatically  $d\sigma/dT < 0$ , as required by the thermal activation process. At the very highest strain rates considered here, however,  $\beta > 0$  may not always be satisfied. So it is explicitly required that  $\beta > 0$ , which implies that this

version of the model is applicable for strain rates  $\dot{\varepsilon} < e^{\beta_0/\beta_1}$ . It is also needed to include pressure hardening, which is accomplished with an overall  $G/G_0$  multiplier. Hence, the modified Zerilli–Armstrong model ( $Z-A_1$ ) is written as

$$\sigma = [c_0 + K\varepsilon^n + Be^{-(\beta_0 - \beta_1 \ln \dot{\varepsilon})T}] \frac{G(P,T)}{G_0} \quad (7)$$

for strain rates up to (but not exceeding)  $\dot{\varepsilon} = e^{\beta_0/\beta_1}$ . Note, for low strain rates,  $\beta_0 \gg \beta_1 \ln \dot{\varepsilon}$ , the  $Z-A_1$  strength in equation (7) becomes independent of strain rate. At very high strain rates,  $\beta = \beta_0 - \beta_1 \ln \dot{\varepsilon}$  becomes small, and a first order Taylor expansion of the exponential in equation (7) leads to  $\sigma \propto \ln \dot{\varepsilon}$ . The PTW model (equation (5)) and the hybrid S–L model (equation (4a)) display similar limiting behaviour before the onset of phonon drag. Hence, there is good consistency between the models over the ranges where they are mutually applicable. Note, linear dislocation drag was added to the  $Z-A$  model for fcc metals in a manner which could be extended to bcc metals.<sup>9</sup>

The models discussed above are illustrated in Fig. 1b as a function of strain rate for Ta at  $P=0.5$  Mbar,  $T=500$  K and  $\varepsilon=0.1$ . The broken curve labelled ‘S- $L_0$ ’ corresponds to the nominal S–L model (equation (4)), including the S–L cap on  $\sigma_T$  when  $\sigma_T > \sigma_P$  with nominal input parameters for Ta.<sup>13</sup> The broken curve labelled ‘S- $L_1$ ’ corresponds to the S–L model with the artificial cap on  $\sigma_T$  removed, allowing the linear phonon drag term to activate. Curves S- $L_1$  and S- $L_0$  coincide in the thermal activation regime for  $\dot{\varepsilon} < 10^5$  s<sup>-1</sup>. At higher strain rates,  $\dot{\varepsilon} > 10^6$  s<sup>-1</sup>, the nominal S–L model, curve ‘S- $L_0$ ’, transitions to essentially the Steinberg–Guinan model (equation (3)), which is strain rate independent. Note, for the S- $L_1$  model at high strain rates, where phonon drag dominates flow stress, as shown by curve ‘S- $L_1$ ’ in Fig. 1b,  $\sigma_T \gg \sigma_{Af}(\dot{\varepsilon})$  in equation (4a), and strength is predicted to be essentially independent of the initial microstructure and work hardening. The solid curve labelled ‘PTW’ in Fig. 1b corresponds to the PTW model (equation (5)), with nominal input parameters for Ta (Ref. 15). In the low strain rate regime,  $\dot{\varepsilon} < 10^5$  s<sup>-1</sup>, PTW also agrees with the S–L models. This is not surprising, because the parameters for both models were calibrated with similar Hopkinson bar data. Using the nominal input parameters for Ta, the PTW model transitions to phonon drag at a higher strain rate,  $\sim 10^8$  s<sup>-1</sup>, owing to the higher reference strain rate  $\dot{\xi}$  ( $\propto$  attempt frequency). The transition is to a power law, nonlinear phonon drag model,<sup>16</sup> with a softer dependence on strain rate,  $\sigma \propto \dot{\varepsilon}^{1/4}$ , based on overdriven shock data. The S- $L_2$  model (equation (4), with  $m=4$  and no cap on  $\sigma_T$ ) is shown in Fig. 1b by the broken curve S- $L_2$ . Here, the reference strain rate (which is proportional to attempt frequency)  $\dot{\varepsilon}_0$  has been increased by  $\sim 100 \times$  over the nominal value. Under these settings, the S- $L_2$  model is consistent with the PTW model over essentially the entire strain rate range.

Finally, the results of the modified Zerilli–Armstrong model (equation (7)) are shown in Fig. 1b by the broken curve labelled  $Z-A_1$ . For nominal input parameters for this model for Ta, the thermal activation regime extends to the low  $\times 10^7$  s<sup>-1</sup> strain rate regime, and over this range, it agrees very well with the PTW model. As described in<sup>7,8</sup> this model addresses deformation in the

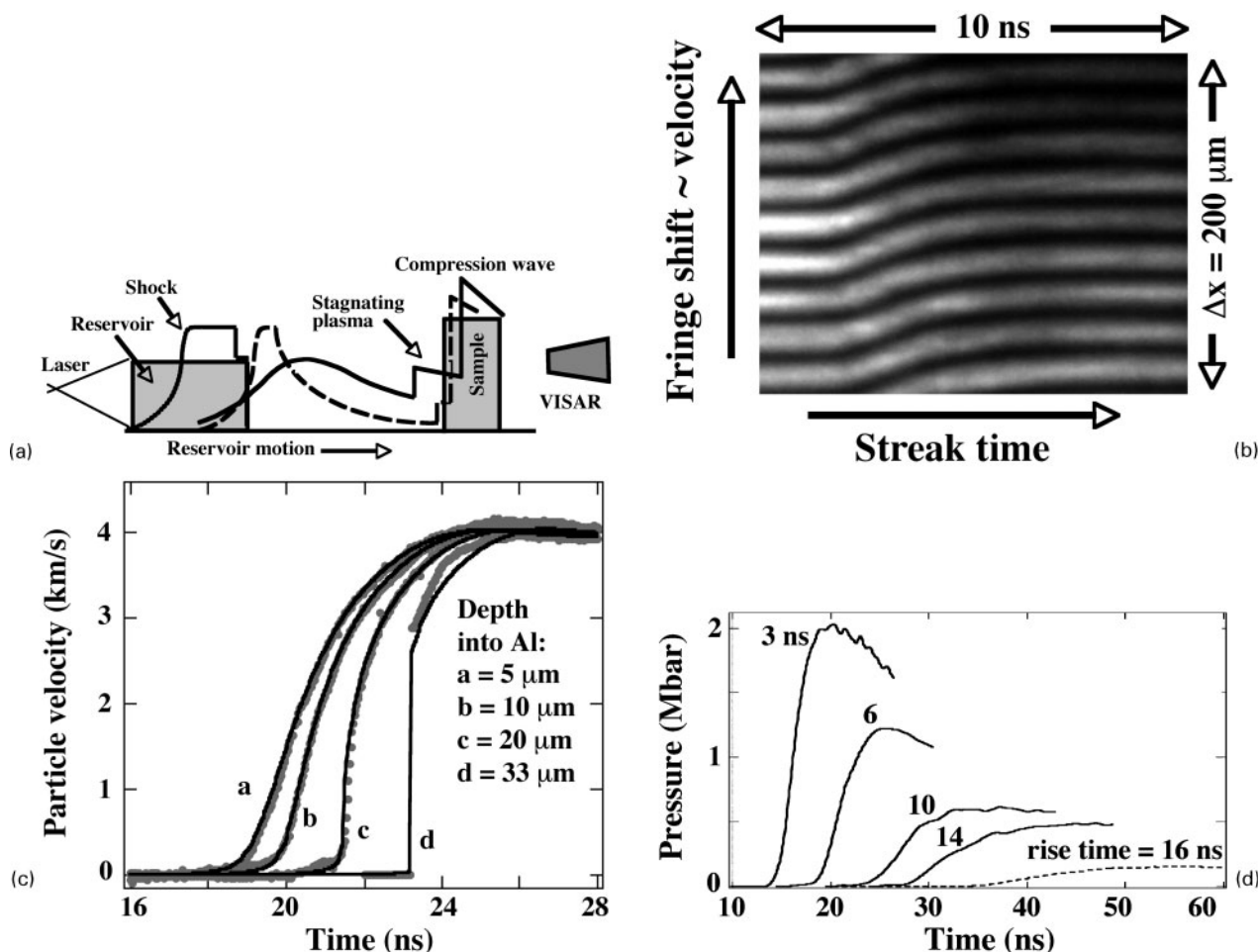
thermal activation regime. Zerilli and Armstrong pointed out nearly two decades ago, however, that to extend to higher strain rates one should address the increase of dislocation density, as opposed to treating  $\rho_m$  as a material constant.<sup>7</sup> This is a key point, which remains to be addressed in future constitutive models addressing high strain rate deformation. In summary, all the models essentially agree, with reasonable parameter settings, in the thermal activation regime. At the highest strain rates, where thermal activation is thought to no longer apply, the models diverge significantly. New data will be needed to test the models in this ultrahigh strain rate regime.

The sensitivity of the PTW model to temperature is illustrated for nominal input parameters for Ta, and starting parameters of  $P=0.5$  Mbar,  $\rho/\rho_0=1.1$  and  $\varepsilon=0.1$ . The flow stress versus strain rate is shown in Fig. 1c, as temperature is increased and decreased by 20 and 40% about a nominal value of  $T_0=500$  K. In the thermal activation regime, assumed here to correspond to  $d\varepsilon/dt < \sim 10^8$  s<sup>-1</sup>, the flow stress shows sensitivity to these levels of changes in temperature. In the phonon drag regime, however, flow stress is rather insensitive to these levels of changes in temperature. The input parameters to the PTW model, including the parameters for phonon drag, are assumed constant. The phonon drag coefficient should in fact increase with temperature and compression as  $D \sim (\rho/\rho_0)^{2/3} T^{1/2}$ , owing to the increasing density of phonons.<sup>3,23</sup> This still would leave the PTW flow stress in the phonon drag regime reasonably insensitive to 20–40% variations in temperature.

Further variation within the PTW model is illustrated in Fig. 1d for Ta at  $P=0.5$  Mbar,  $T=500$  K and  $\varepsilon \approx 0$ , as the input parameters  $\gamma$  and  $y_0$  are varied. The results are shown from decreasing both  $\gamma$  and  $y_0$  together, holding  $y_\infty$  fixed. This effectively lowers the Peierls stress ( $\sigma_P = y_0 - y_\infty$ ), as the mobile dislocation density ( $\rho_m \sim \gamma$ ) is decreased. The result is that the flow stress in the thermal activation regime (solid curves) remains roughly the same, but transitions to the phonon drag regime (broken curves) at lower strain rates. This sharply increases the flow stress at the highest strain rates, while leaving flow stress unchanged at the lower strain rates, where the models are well constrained by Hopkinson bar data. When flow stress from the PTW model is examined *v.* strain (not shown), it can be seen that strain hardening does not affect flow stress in the phonon drag regime. In this regime, the dislocations are assumed to be gliding above the barriers, so that work hardening owing to the accumulation of microstructure has little effect on flow stress. This prediction remains to be tested by experiment.

## Shockless drive development

This section discusses the results of an experimental technique for generating a very high pressure, high strain rate ‘drive’ to compress samples in the solid state. This technique has been experimentally demonstrated up to peak pressures of 200 GPa (2 Mbar) at the Omega laser.<sup>24</sup> Furthermore, radiation hydrodynamics simulations show that on future facilities, such as the NIF laser,<sup>4</sup> this technique should be able to drive samples in the solid state to much higher pressures,  $P > 10^3$  GPa (10 Mbar) (Ref. 5).



a schematic illustrating how laser driven ramped drive works; b VISAR trace of  $P_{\max}=1.2$  Mbar ramped drive laser shot on the Omega laser; c the analysis of a series of 1.2 Mbar ramped drive experiments at Omega, varying the thickness of the Al sample; laser energy and intensity used were  $\sim 1.2$  kJ and  $4.5 \times 10^{13}$  W cm $^{-2}$ ; d pressure v. time for five different experiments at Omega, showing ramped drive for maximum pressures spanning 0.15 Mbar–2 Mbar; conditions for highest pressure shot were  $P_{\max} \sim 2$  Mbar peak pressure,  $\rho/\rho_0 \sim 2$  compression,  $E_L \sim 2$  kJ total drive laser energy, and  $I_L \sim 8 \times 10^{13}$  W cm $^{-2}$  laser intensity on target<sup>24,25</sup>

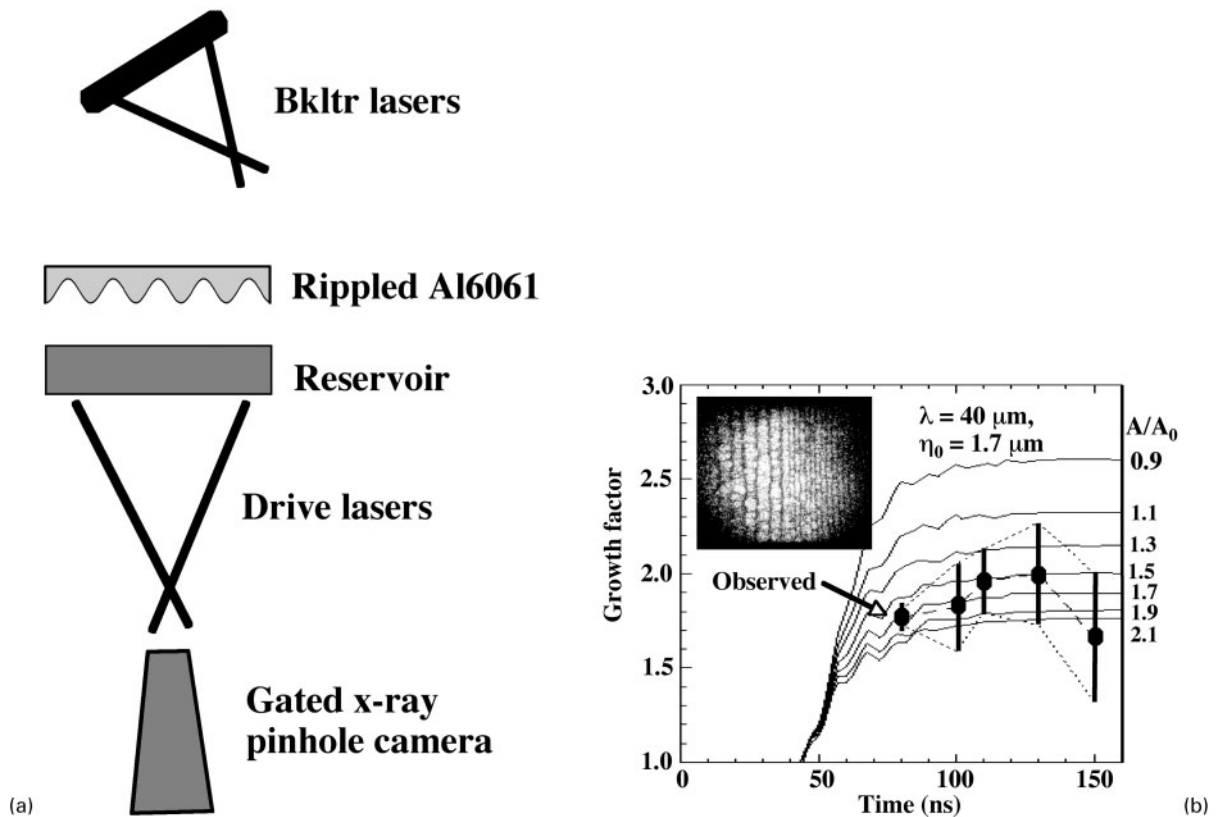
## 2 Ramped drive

Results from this ramped pressure shockless drive<sup>24,25</sup> that has been developed on the Omega laser are shown in Fig. 2.<sup>26</sup> The target consists of a low Z, low density reservoir (typically solid density plastic) of nominal thickness  $\sim 0.2$  mm, followed by an  $\sim 0.3$  mm vacuum gap, then an Al sample, as illustrated schematically in Fig. 2a. A laser pulse of energy 0.2–2 kJ in a temporally square pulse shape of duration 3–4 ns is used to drive a strong shock through the low Z reservoir. When the shock reaches the back side (the side opposite where the laser was incident), the reservoir ‘explodes’ (unloads) into vacuum as a gas of ‘ejecta’. The pressure that is applied to the sample results from the increasing ram pressure,  $P_{\text{ram}} = \rho_{\text{ejecta}} v_{\text{ejecta}}^2$ , which increases smoothly and monotonically in time as the reservoir unloads, until the reservoir material is depleted. This technique for generating shockless compression was modelled after the early work of Barnes using high explosives (HE) as the source of the shock in the reservoir.<sup>27,28</sup>

The pressure wave is measured with a velocity interferometer<sup>29</sup> viewing the back side of a 5–30  $\mu\text{m}$  thick flat Al sample, typically through a LiF window. An example VISAR image, corresponding to a 5  $\mu\text{m}$  Al sample backed by an  $\sim 125$   $\mu\text{m}$  LiF window, where  $P_{\max}$

$\sim 1.2$  Mbar, is shown in Fig. 2b (Ref. 24). The horizontal direction on the image is the ‘streak’ or time direction, and the vertical direction corresponds to the transverse position along the sample. The interference fringes in the velocity interferometer diagnostic are proportional to velocity, with each fringe shift,  $\delta$  (fringe position), corresponding to a known velocity increment  $\delta v$ . Therefore, measuring the fringe shift versus time and position on the foil is a direct measure of the velocity of the reflecting surface or interface, if a LiF window is used. As this ramp wave moves through the Al, it eventually steepens into a shock, as illustrated experimentally and numerically in Fig. 2c. The grey symbols are the experimental data, and the solid curves are radiation hydrodynamics continuum code simulations. Here, a set of four identical laser shots was done at the Omega laser, each at  $P_{\max} \sim 1.2$  Mbar, where the only difference was the Al thickness, which varied over 5–33  $\mu\text{m}$ . By the time this 1 Mbar ramp wave has moved through  $\sim 30$   $\mu\text{m}$  of Al, it has steepened into a shock.

The measured velocity profiles can be back integrated to infer the applied pressure v. time at the front surface of the Al sample, using a technique developed by Hayes.<sup>30</sup> The results from five different experiments are



**a** experimental configuration for using the ramped drive at the Omega laser for an RT instability experiment at high pressure, solid state conditions; unloading reservoir pushes on rippled thin metal payload; **b** examples of a series of RT experiments in Al6061-T6 to infer strength at  $P_{\max}=200$  kbar; 2D simulations used the Steinberg–Guinan strength model, and varied pressure hardening term multiplier  $A$ , until results reproduced experimental observations<sup>34</sup>

### 3 Rayleigh–Taylor instability as a strength diagnostic

shown in Fig. 2d, varying mainly the laser intensity, leading to peak pressures spanning 15–200 GPa (0.15–2 Mbar). As the peak pressure increases, the pressure rise time decreases. Nevertheless, even at 2 Mbar, with an  $\sim 3$  ns rise time, the sample is not shocked, at least over the first 10–20  $\mu\text{m}$  of Al (Ref. 24).

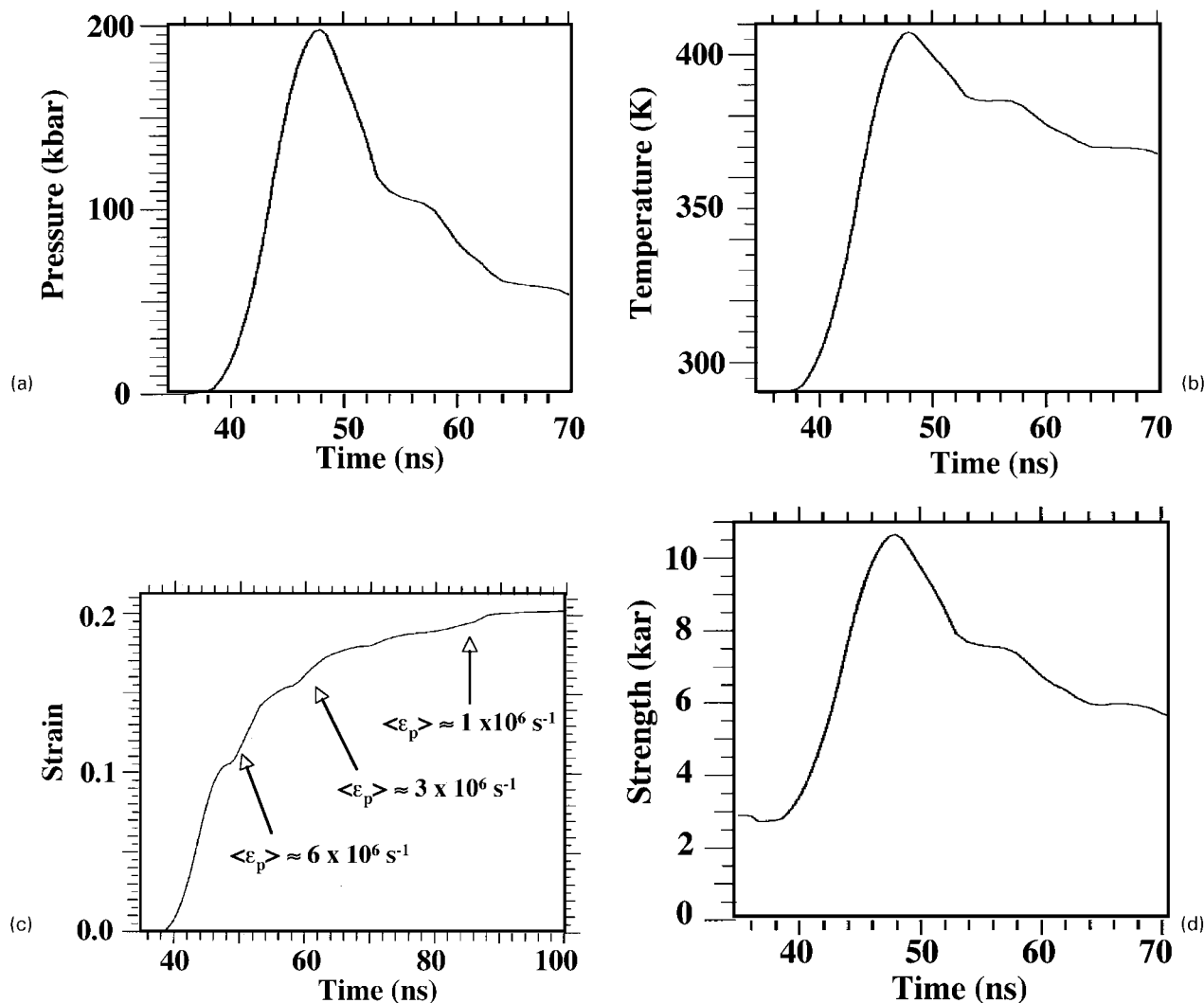
## Material strength at high pressure and strain rate

To dynamically infer material strength at high ( $P$ ,  $d\varepsilon/dt$ ), hydrodynamic instability experiments have been developed,<sup>3,31–34</sup> following the pioneering work by Barnes.<sup>27,28</sup> By accelerating a metal sample or payload with a high pressure, low density ‘pusher’, a situation is created where the interface with the payload is hydrodynamically unstable to the Rayleigh–Taylor (RT) instability. Any pre-existing perturbations will attempt to grow, whereas material strength will act to counter or slow this growth. By measuring the RT growth of machined sinusoidal ripples in metal foils that are accelerated by the drive, and comparing the observed perturbation growth with that from simulations including a constitutive strength model, material strength at high pressure and strain rate may be inferred.

The technique being developed to test models of high pressure and dynamic strength, such as represented by equation (1–5), is to measure the RT induced growth of ripples with time resolved face-on radiography, as illustrated schematically in Fig. 3a. We use the ramped

pressure drive discussed in Fig. 2 to generate both high pressure conditions in the sample of interest, and to accelerate the sample. Preimposed ripples on the side of the metal sample facing the reservoir then are induced to grow owing to the RT instability. The RT instability exerts a shear stress on the sample, as material flows plastically from the thin regions or valleys of the perturbations (RT ‘bubbles’) to the thick regions or peaks of the perturbations (RT ‘spikes’). The material strength at the high pressures and strain rates generated attempts to resist this plastic flow. Hence, the rate at which the ripples grow is sensitive to the material strength; the stronger the material, the lower the expected RT growth rate. Comparing 2D hydrodynamic simulations, including a strength model, with the observed RT growth rates, allows the model to be tested, and the high pressure strength to be deduced.

Figure 3b shows results from such a RT experiment, in this case, for Al6061-T6 foils at  $P_{\max} \sim 20$  GPa (200 kbar). The data for perturbation growth factor versus time are given by the plotting symbols, and the results of the 2D simulations, using the Steinberg–Guinan strength model (equation (4)) are given by the solid curves. The pressure hardening parameter,  $A = \frac{1}{G_0} \frac{\partial G}{\partial P}$ , is varied in the model until the simulations reproduce the observations. At peak pressure, the deduced strength from the best fit simulation, is 10.5 kbar, at  $P_{\max} \sim 200$  kbar and peak strain rate of  $\sim 6 \times 10^6 \text{ s}^{-1}$  (Ref. 34). Using the simulation that reproduced the experimentally observed RT growth



a average pressure *v.* time, showing maximum of  $\sim 200$  kbar at  $t = 48$  ns; b average temperature *v.* time, starting from room temperature and showing peak of  $\sim 400$  K at time of peak pressure (48 ns); after peak, temperature does not decrease as quickly as pressure *v.* time, owing to irreversible heating from plastic work of compression and deformation, and owing to the heat wave moving into sample from the drive (see text); c plastic strain  $\epsilon_p$  *v.* time; average slope as function of time gives estimate of strain rate; values of strain rate range from  $d\epsilon_p/dt \sim 6 \times 10^6 \text{ s}^{-1}$  early in drive to  $d\epsilon_p/dt \sim 1 \times 10^6 \text{ s}^{-1}$  at late times; d average strength *v.* time; at its maximum, strength has increased by a factor of  $\sim 4$ , largely owing to pressure hardening<sup>35</sup>

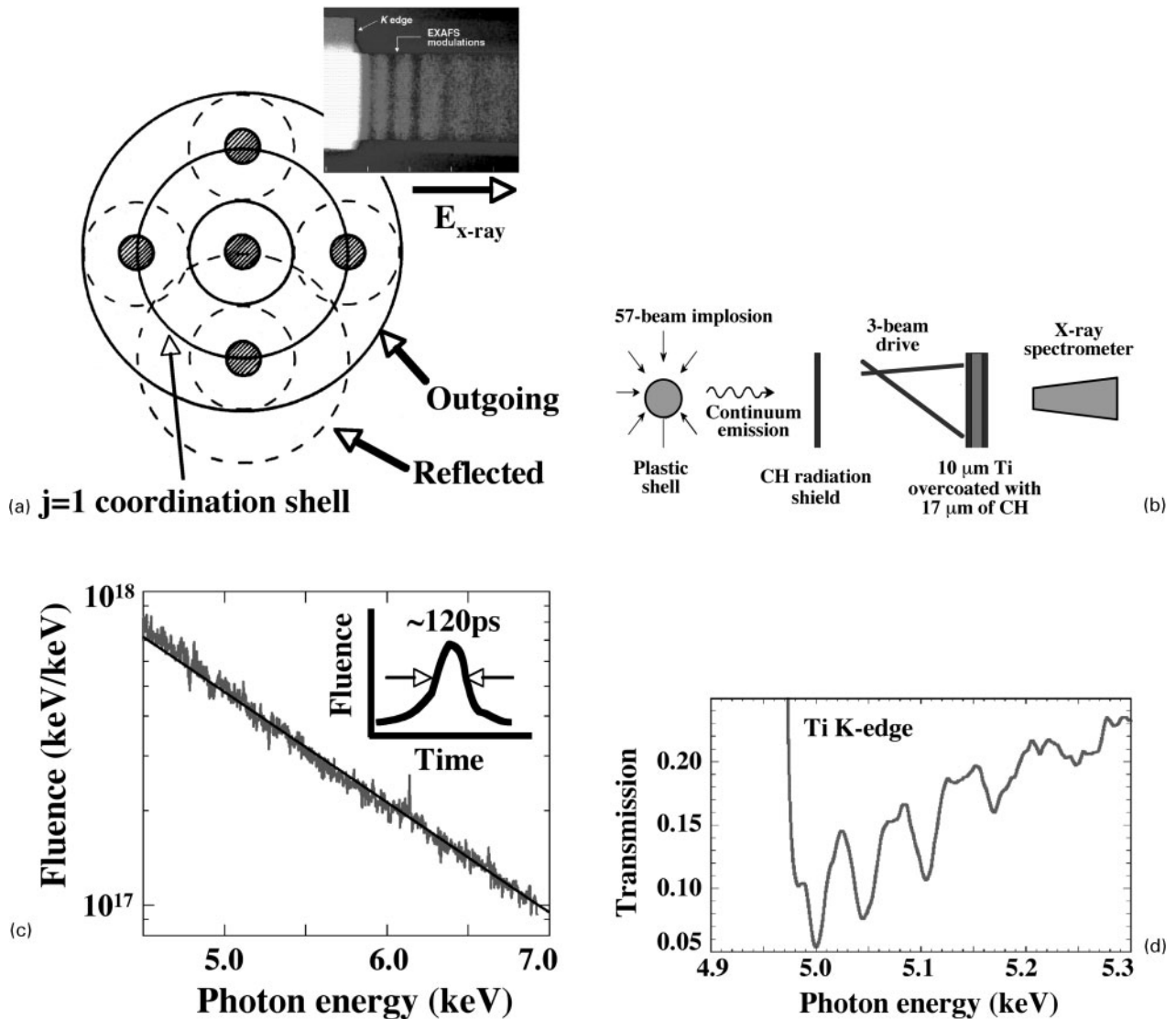
4 Parameters from 2D RT simulations, volume averaged over foil dimensions, assuming  $e^{-kz}$  weighting, where  $k=2\pi/\lambda$  is perturbation wave vector (see text)

shown in Fig. 3b, then the time histories of pressure (Fig. 4a), temperature (Fig. 4b), equivalent plastic strain (Fig. 4c) and flow stress (Fig. 4d). The results have been volumetrically averaged with  $e^{-kz}$  weighting, where  $k=2\pi/\lambda$  corresponds to the perturbation wave number. This particular weighting is based on the recognition that the strength that matters is that in the vicinity of the growing ripples. Because RT induced ripples penetrate the foil a distance of order  $e^{-kz}$ , where  $k=2\pi/\lambda$  is the perturbation wave number, we have used  $e^{-kz}$  weighting in the averages shown in all the plots in Fig. 4. The average peak pressure (Fig. 4a) was  $\sim 200$  kbar with an  $\sim 6$  ns rise time. The temperature starts out a room temperature and increases to a peak value of  $\sim 400$  K, as shown in Fig. 4b. The equivalent plastic strain from the simulation is shown in Fig. 4c, and asymptotically reaches  $\epsilon_p \sim 0.2$ . By looking at the average values of the slope at various time intervals, average plastic strain rates can be estimated. Early in

time (40–55 ns), the average strain rate is  $(d\epsilon_p/dt) \sim 6 \times 10^6 \text{ s}^{-1}$ . At later times, 55–70 ns, as the applied pressure drops off, the strain rate also decreases,  $(d\epsilon_p/dt) \sim 3 \times 10^6 \text{ s}^{-1}$ . At still later times, 70–90 ns, the strain rate approaches  $(d\epsilon_p/dt) \sim 1 \times 10^6 \text{ s}^{-1}$ . The volume averaged strength is shown in Fig. 4d. The peak value is 10.5 kbar, which is a factor of  $10.5/2.9$ ,  $\sim 3.5$  larger than the strength under ambient conditions, owing largely to the pressure hardening effect.<sup>35</sup> This is the approach being pursued to test high pressure, high strain rate models of material strength, at extremely high pressures. One key sensitivity still being examined is the 2D effects (such as foil bowing) on the drive,  $P(t)$ , especially at late times. Our conclusions about high pressure strength are only as good as our understanding of the drive.

## Dynamic EXAFS experiments

A time resolved microscale diagnostic developed to probe the local lattice response, namely, dynamic EXAFS is now



a physics basis for EXAFS process; b experimental configuration for dynamic EXAFS technique, developed at Omega laser; c X-ray spectrum emerging from capsule implosion, used for EXAFS transmission measurements; note, X-ray burst duration is very short, lasting only  $\sim 120$  ps; d modulations above K edge of cold Ti in EXAFS demonstration experiment<sup>39</sup>

## 5 Extended X-ray absorption fine structure measurement technique

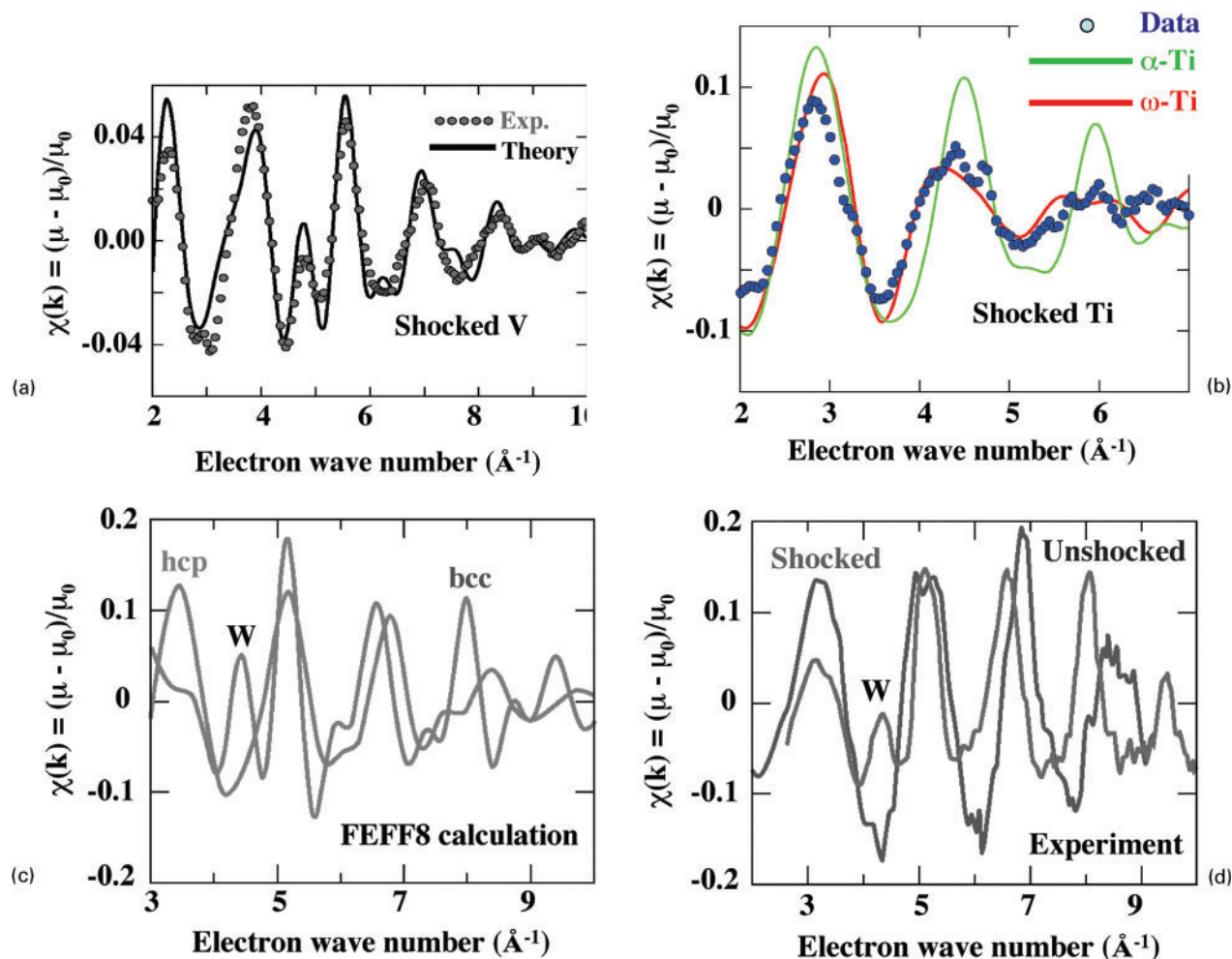
discussed. This EXAFS technique probes the lattice short range order, works both with polycrystalline or single crystal samples, and offers the potential to infer phase, compression, and temperature of the loaded sample, with subsec time resolution. The basis for this diagnostic is illustrated in Fig. 5a (Ref. 36–38). When an atom absorbs an ionising, high energy X-ray, an electron rises from a bound state into the continuum. The outgoing wave packet of the free electron, illustrated by the concentric solid circles in Fig. 5a, scatters off of neighbouring atoms, as illustrated by the broken circular curves. The outgoing and reflected waves interfere with each other. The square of the total electron wave function is what determines the probability of the process, and this interference is therefore observed in fine structure in the X-ray absorption just above an opacity edge. For K edge absorption, the standard EXAFS equation can be written, in terms of the normalised absorption probability, as<sup>36,39–41</sup>

$$\chi(k) = \sum_j \frac{N_j}{kR_j^2} F_j(k) \sin\{2kR_j + \phi_j(k)\} e^{-2\sigma_j^2 k^2} e^{-2R_j/\lambda(k)} \quad (9)$$

where  $\chi(k) = [\mu(k) - \mu_0(k)]/\mu_0(k)$ , and  $\mu_0(k)$  represents

the smooth absorption above the edge corresponding to an isolated atom (no interference modulations). The summation is over coordination shells,  $N_j$  is the number of atoms in the shell and  $R_j$  its radius. The  $F_j(k)$  factor corresponds to the backscattering amplitude for the electron wave function reflected from the  $j$ th coordination shell. The  $\phi_j(k)$  represents a phase shift owing to the electron wave packet moving through a varying potential. The exponential  $e^{-2\sigma_j^2 k^2}$ , represents amplitude damping owing to the Debye–Waller factor, which reduces the coherent interference of the EXAFS signal owing to thermal and static disorder fluctuations in the local scattering atoms. The  $e^{-2R_j/\lambda(k)}$  factor represents the attenuation of the electron wave function owing to the finite mean free path  $\lambda(k)$  of the ejected electron.

The time resolved EXAFS diagnostic technique has been developed at the Omega laser.<sup>39–41</sup> The experimental set-up is shown in Fig. 5b. Three 1 ns square laser beams stacked back to back to make a 3 ns square drive pulse are used to shock compress the sample being studied. In Fig. 5b, the sample corresponds to a 10  $\mu\text{m}$  thick foil of polycrystalline Ti embedded in 17  $\mu\text{m}$  thick

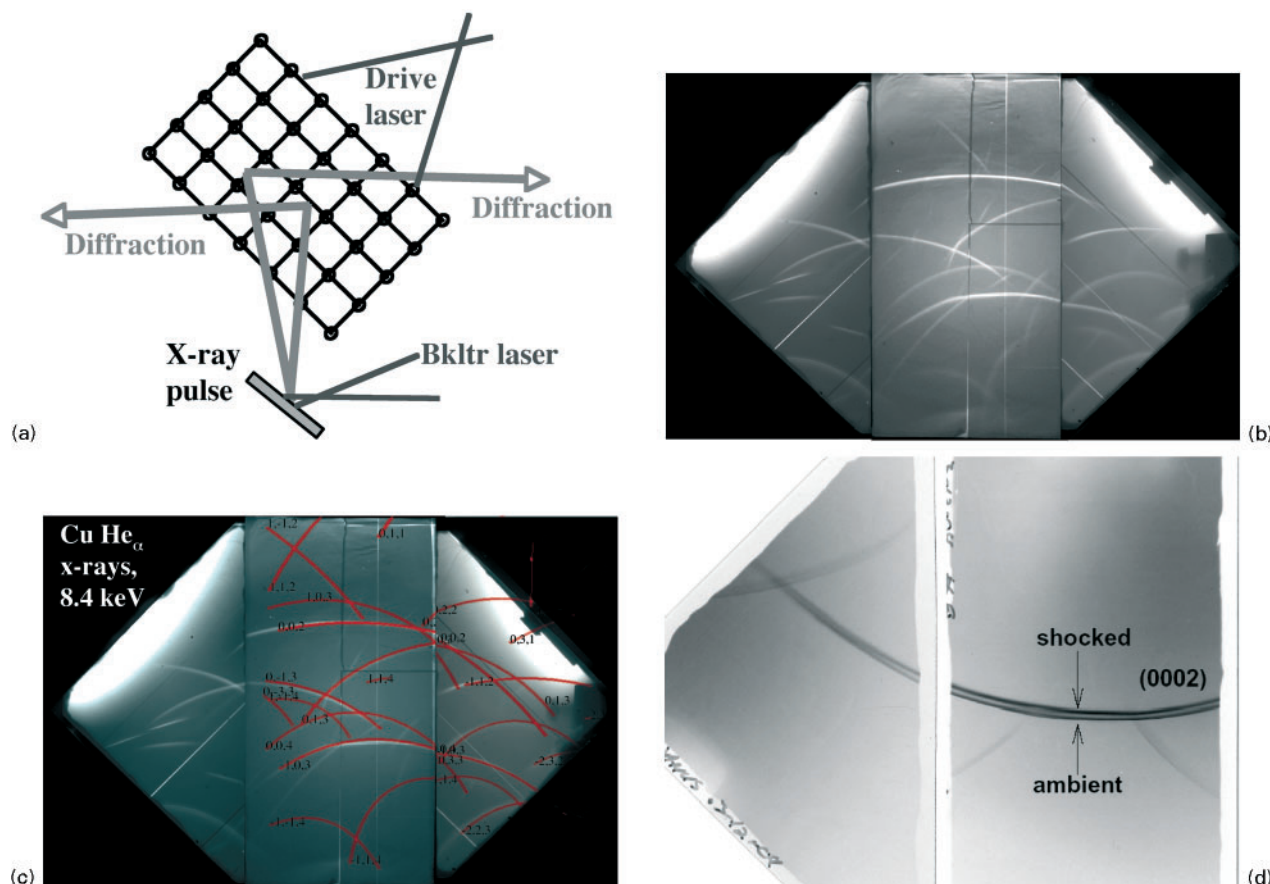


6 Extended X-ray absorption fine structure results for *a* shocked V ( $P_{\text{shk}} \sim 450$  kbar,  $\rho/\rho_0 = 1.15$ ,  $T = 770$  K, no phase transition observed); *b* shocked Ti, at  $P_{\text{shk}} \sim 350$  kbar,  $\rho/\rho_0 = 1.2$ , and  $T = 900$  K;  $\alpha \rightarrow \omega$  phase transition is observed at transition time scale of  $\delta t < \sim 1$  ns; smooth curves correspond to variety of fits using EXAFS theoretical code, FEFF8 (see text); *c* FEFF8 simulations of EXAFS from unshocked and shocked Fe at  $P_{\text{shk}} \sim 350$  kbar;  $\alpha$  phase (bcc), for unshocked Fe and  $\epsilon$  phase (hcp) for shocked Fe are shown; and *d* dynamic EXAFS measurements of unshocked and shocked Fe at  $P_{\text{shk}} = 350$  kbar;  $\alpha \rightarrow \epsilon$  phase transition is experimentally observed, for transition time scale of  $\delta t < \sim 1$  ns (Ref. 40–44)

CH tamper on either side, and the remaining 57 beams implode an inertial confinement fusion (ICF) capsule. This implosion generates a short ( $\sim 120$  ps) burst of (spectrally) smoothly varying hard X-rays,  $I = I_0 \exp(-E_x/T)$ , to be used for the EXAFS absorption, as shown in Fig. 5c. Typical values for the implosion X-ray spectrum are  $I_0 = 2 - 3 \times 10^{19}$  keV/keV and  $T = 1.25$  keV. A measured raw EXAFS absorption spectrum showing the modulations just above the K edge for room temperature, unshocked polycrystalline Ti is shown in Fig. 5d (Ref. 39).

Measurements of EXAFS from shocked polycrystalline vanadium at  $P_{\text{shk}} \sim 400$  kbar, together with EXAFS theoretical fits, using the FEFF8 code,<sup>38,40,41</sup> are shown in Fig. 6a. Vanadium was picked as a good reference material, because it is not expected to undergo any phase transition at shock pressures  $< \sim 1$  Mbar. The fits of the shocked V EXAFS data with the FEFF8 code shown in Fig. 6a are very good, and suggest a compression of  $\sim 15\%$  and shock temperature of  $\sim 800$  K. Both the shock compression and shock temperature thus inferred are in good agreement with predictions with radiation hydrodynamics code simulations using the LASNEX code.<sup>42</sup>

Having established the technique of dynamic EXAFS to diagnose shocked samples with subsec time resolution, the technique is then applied to shocked polycrystalline Ti, at the same  $P_{\text{shk}} \sim 400$  kbar, as shown in Fig. 6b. In this case, the situation is distinctly different from the shocked V. If we assume that the shock temperature is the same as for shocked V, and fit the FEFF8 simulation to reproduce the modulation period, assuming no phase transition, the result is shown as the thin grey curve. This fit is clearly unsatisfactory, and suggests this interpretation cannot be correct. If we again assume no phase transition, but arbitrarily increase the temperature until the theoretical curve fits the data, the resulting temperature is  $T \sim 2100$  K. This temperature is over a factor of two higher than predicted with the LASNEX simulations and in distinct disagreement with the temperatures inferred from the shocked V at the same shock strength. It is concluded that such a high temperature is unphysical. If, on the other hand, the shocked Ti has undergone the  $\alpha \rightarrow \omega$  phase transition, as expected for these pressures, and assuming the nominal shock temperatures from the radiation hydrodynamics simulations of  $T \sim 900$  K, the result is shown by the thick black curve in Fig. 6b. The agreement with



**a** experimental configuration for laser based dynamic diffraction;<sup>49</sup> **b** example of dynamic diffraction on unshocked single crystal Cu;<sup>50</sup> **c** same as **b** only with fits overlaid corresponding to Bragg diffraction from various lattice planes and from crystal diffraction analysis off the static (uncompressed) sample;<sup>50</sup> **d** example of dynamic diffraction from shocked single crystal Ti, shocked along [0002] on Janus laser at  $P_{\text{shk}}=6.9$  GPa<sup>52,53</sup>

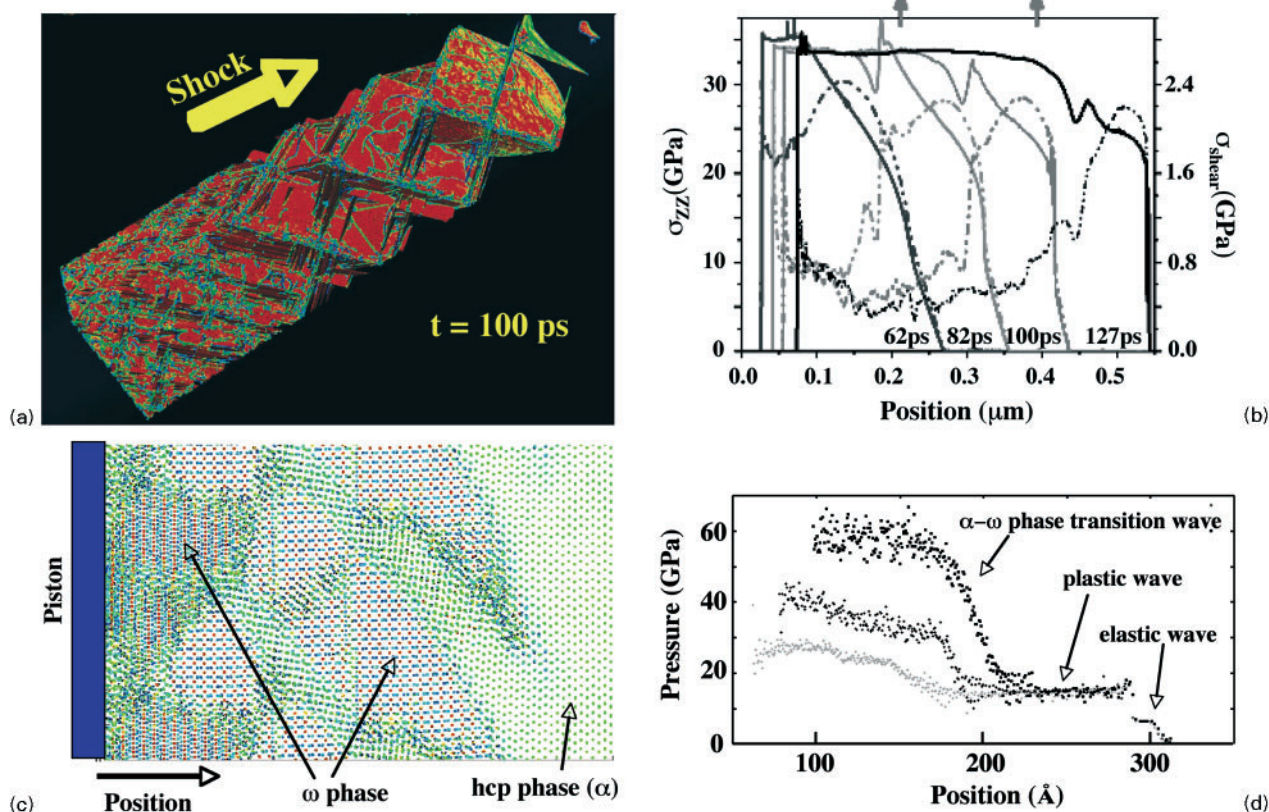
## 7 Dynamic diffraction technique

the data is excellent, and it is therefore concluded that this is the most likely interpretation. It is thus concluded that at  $P_{\text{shk}} \sim 400$  kbar, the time scale for the  $\alpha-\omega$  phase transition is prompt,  $\delta t_{\alpha-\omega} < 1$  ns.

Next, shocked polycrystalline Fe is probed with this dynamic EXAFS technique.<sup>43,44</sup> The FEEF8 theory was first used to establish the expected EXAFS spectra for unshocked  $\alpha$  phase (bcc) Fe and shocked  $\epsilon$  phase (hcp) Fe, assuming a  $\sim 20\%$  compression for the shocked state, as shown in Fig. 6c. A 20% compression is predicted from radiation hydrodynamics simulations of shocked Fe at  $P_{\text{shk}} \sim 350$  kbar, assuming the  $\alpha-\epsilon$  phase transition. Figure 6c clearly shows that the small peak marked 'w' in the  $\alpha$  phase disappears in the  $\epsilon$  (hcp) phase. The dynamic EXAFS results of the shocked Fe experiments are shown in Fig. 6d; the 'w' peak is unmistakably absent. Based on the comparison of Figs. 6d with c, it is concluded that the  $\alpha-\epsilon$  phase transition of shocked Fe has been observed, and that the transition time scale (at  $P_{\text{shk}} \sim 350$  kbar) is subsec.<sup>43,44</sup> Dynamic diffraction experiments of shocked Fe at the Omega laser have also shown that this transition occurs on subns time scales at  $P_{\text{shk}} \sim 350$  kbar.<sup>45-47</sup> In addition, the shocked Fe diffraction experiments showed that the compression path was from 1D  $\alpha$  phase (bcc) to 3D  $\epsilon$  phase (hcp), with no observation of a 3D, plastically relaxed  $\alpha$  phase preceding the phase transition. The earlier MD simulations had actually predicted this exact lattice response.<sup>48</sup>

## Dynamic diffraction experiments

Time resolved dynamic diffraction experiments are now discussed. This technique offers the potential to probe fundamental quantities such as phase, Peierls barrier and dislocation mobility at high pressures and strain rates, and is particularly well suited to studies of shocked single crystals. If a shock or compression wave traverses a single crystal, the lattice planes compress, and potentially relax through plastic flow towards a more 3D symmetric (hydrostatic) configuration. This can be observed by recording Bragg diffraction signals off multiple lattice planes, as illustrated in the sketch in Fig. 7a (Ref. 49). The shock compressed lattice can be measured by recording the diffraction signal from a short ( $\sim 1$  ns) synchronised point source burst of X-rays, onto X-ray film. An example of an unshocked diffraction experiment in single crystal Cu, done at the Vulcan laser at RAL, England, is shown in Fig. 7b.<sup>50</sup> The same data, with  $\sim 10$  lattice planes identified by fitting with a crystal diffraction code, is shown in Fig. 7c. The agreement between observation and prediction is excellent. The (laser driven) X-ray source was Cu He $_{\alpha}$  at 8.3–8.4 keV. Even though this is unshocked, the image in Fig. 7c shows the power of dynamic diffraction for determining the phase of the sample, with subsec time resolution. We have also done dynamic diffraction experiments with shocked Cu, at  $P_{\text{shk}} \sim 180$  kbar<sup>51</sup> The conclusion from the dynamic experiments was that the



*a* a very large scale MD result of shocked single crystal Cu with embedded pre-existing dislocation sources; simulated shock had 50 ps linear ramp rise time;<sup>54</sup> *b* analysis of MD result given in *a*, showing stress along shock direction  $\sigma_{zz}$  and shear stress  $\sigma_{\text{shear}}$  (lower curves); vertical arrows indicate location of pre-existing dislocation sources, which give local shear stress different from zero even in pre-shocked material; curves correspond to 62 ps, 82 ps, 100 ps and 127 ps; homogeneous nucleation starts at  $\sim 53$  ps after leading edge of pressure pulse; *c* result of MD simulations of shocked single crystal Ti, at  $P_{\text{shk}} \sim 220$  kbar; colours represent coordination number; *d* pressure versus position for shocked Ti MD simulation shown in *c*; note 3 wave structure: elastic, plastic and phase transition wave<sup>56</sup>

## 8 Molecular dynamics simulations

shocked Cu sampled relaxed to a 3D symmetric (hydrostatic) state promptly, i.e., over subnsec time scales.

An example from a dynamic driven experiment is shown in Fig. 7*d* for single crystal Ti shocked along the [0001] direction at  $P_{\text{shk}} \sim 70$  kbar, performed on the Janus laser at LLNL.<sup>52</sup> Initially there is diffraction only from the unshocked region (lower arc, labelled 'ambient'). Later in time, there are regions of the Ti that have been shocked, and regions that remain unshocked. With a laser driven, doubled pulsed 'back lighter', i.e. timed burst of X-rays, both shocked and unshocked regions can be superposed on the same film pack, as shown in the image in Fig. 7*d*. Ongoing dynamic diffraction experiments over a range of shock strengths in Ti are attempting to confirm the  $\alpha$ - $\omega$  phase transition inferred from the dynamic EXAFS results. The diffraction experiments are also examining whether the compression is in a plastically relaxed 3D symmetric (similar to hydrostatic) state before the phase transition.<sup>53</sup>

Molecular dynamics simulations offer a very powerful tool for predicting the microscopic lattice response to compression at high pressures and strain rates. Two examples are shown in Fig. 8, corresponding to shocked Cu (Fig. 8*a* and *b*) and shocked Ti (Fig. 8*c* and *d*). The shocked Cu simulation corresponds to a 352 million atom simulation of single crystal Cu  $\sim 1 \mu\text{m}$  thick, shocked at  $P_{\text{shk}} \sim 35$  GPa along the [001] direction.<sup>54</sup> The Cu sample included pre-existing dislocation sources

in the form of prismatic loops, and the shock front had an  $\sim 50$  psec linear ramp. A snapshot from this simulation at 100 ps, showing the centrosymmetry parameter (CSP), is given in Fig. 8*a*. The colour scale has been adjusted to show both dislocations and stacking faults. The shock leading edge is just approaching the pre-existing prismatic loop source at the upper right of the figure. Once the pressure ramp wave exceeds the threshold for either activating the source ( $\sigma_{zz} \sim 10$  GPa) or homogeneous nucleation of dislocations,  $\sigma_{zz} \sim 30$  GPa, a high density of dislocations and stacking faults is created, and the evolution towards 3D plastic relaxation behind the shock front commences. One conclusion from these simulations is that to reproduce the experimentally observed prompt 3D plastic relaxation of shocked single crystal Cu<sup>51</sup> requires very large scale simulations, covering  $\sim 1 \mu\text{m}$  sample thickness and  $\sim 0.2$  ns shock transit time. Shorter simulations show large dislocation densities being created, but do not allow sufficient time for dislocation transport to relax the initially 1D lattice compression to the plastic 3D relaxed state.<sup>55</sup> Analysis of the MD result given in Fig. 8*a*, showing stress along the shock direction and shear stress at various times, is presented in Fig. 8*b*. Vertical arrows indicate the location of the pre-existing dislocation sources. Homogeneous nucleation starts at  $\sim 53$  ps after the leading edge of the pressure pulse. Before the shock wave encounters the pre-existing

source, the dislocation density and relaxation corresponds to homogenous nucleation; the maximum dislocation density from the MD simulation is  $\sim 3 \times 10^{13} \text{ cm}^{-2}$ . Once the pre-existing source has been activated by the ramp wave, the dislocation density drops by a factor of  $\sim 3$ , owing to plastic relaxation commencing at a much lower stress threshold of  $\sim 10 \text{ GPa}$ . This allows greater time for plastic relaxation to occur during the ramp. Hence, with a ramped drive, a greater 3D relaxation is achieved with a lower peak value of dislocation density.<sup>54</sup>

An MD simulation of shocked single crystal Ti is shown in Fig. 8c, at a shock strength of  $P_{\text{shk}} = 22 \text{ GPa} = 220 \text{ kbar}$ , which is well above the experimentally inferred  $12 \text{ GPa}$  shock threshold for observing the  $\alpha$ - $\omega$  phase transition.<sup>40,41</sup> The Ti was shocked along the [0001] direction. The MD simulation shows a very prompt transition from the  $\alpha$  phase to the  $\omega$  phase.<sup>56</sup> Figure 8d shows axial profiles of the pressure wave, showing a dramatic 3 wave structure. The leading elastic (1D compression) wave is observed in this plot at a position of  $\sim 300 \text{ \AA}$ , followed by a plastic relaxation wave at  $\sim 290 \text{ \AA}$ . The  $\alpha$ - $\omega$  phase transition wave trails these two leading waves, commencing at a position of  $\sim 200 \text{ \AA}$ . This situation, which is consistent with the experimental diffraction results shown in Fig. 7d, is different from the shocked Fe case, which evolved directly from 1D compression of the initial phase directly into the phase transition. With the shocked Ti, it appears that the lattice first enters the plastic relaxation regime, and then undergoes the structural phase transition. It will be interesting in subsequent work to understand the precise differences between these two cases.

## Recovery of driven samples

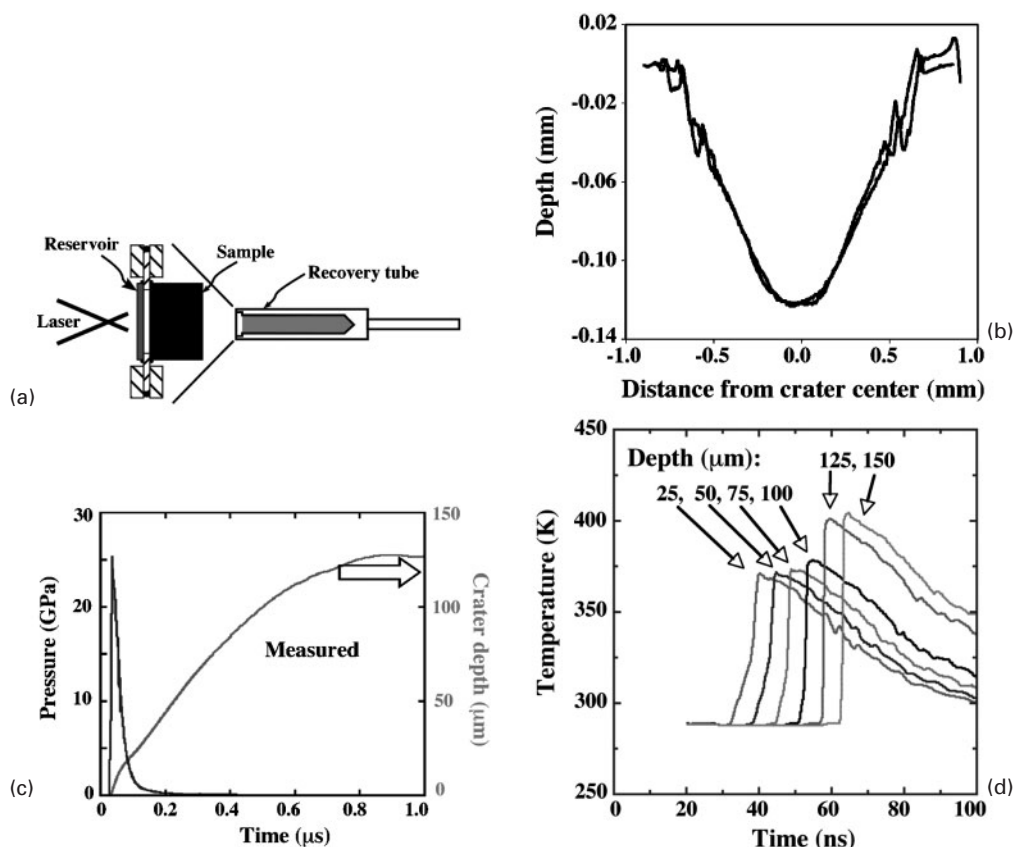
In this section the use of sample recovery to infer deformation mechanisms and integral quantities about the drive and sample is discussed. The experimental configuration for one class of recovery experiments is shown in Fig. 9a. In the ramped drive case illustrated, which is similar to the drives illustrated in Fig. 2, the laser drives a shock through a reservoir, which expands across a gap and stagnates on the sample being studied. The main differences are that the sample is typically much thicker so that it survives the loading process, and it is recovered in a foam filled recovery tube. A substantial number of recovery experiments have also been carried out with a simpler shock drive that results from direct laser illumination of the sample.<sup>2,57,58</sup> In the ramped wave case, as the compression wave runs into the sample, it eventually steepens into a shock, as shown in Fig. 2c. So for recovery experiments involving thick samples and a ramped drive, the portion of the sample nearest the driven surface feels the ramped (shockless) loading, whereas regions deeper into the sample see a shocked drive. The lattice response can vary, depending on whether the load is a ramp or a shock.<sup>59</sup>

In either loading case, the macroscopic end result is the formation of a crater at the driven surface. An example for single crystal Cu ramp loaded to  $P_{\text{max}} \sim 250 \text{ kbar}$  is shown in Fig. 9b (Ref. 59). The crater dimensions are  $\sim 120 \mu\text{m}$  deep with  $\sim 1 \text{ mm}$  diameter, and depend on the strength, duration of the loading and the strength of the material. The dynamics of crater

formation is illustrated in Fig. 9c, based on the results from 2D simulations. Note in particular that the crater formation process is very slow,  $\sim 1 \mu\text{s}$ , compared with the drive duration, which is a few  $\times 10 \text{ ns}$ . The duration of the high pressure ( $250 \text{ kbar}$ ) loading is a few tens of nanoseconds. Behind the loading wave, a slow plastic flow is induced. This plastic flow continues until its energy is dissipated by the strength of the material. The result is that the crater formation is not complete until a microsecond or longer, as shown in Fig. 9c. The temperatures felt, as a function of depth from the loaded surface, are shown in Fig. 9d, from the same simulations that reproduced the observed crater depth. In the shockless region, at depths  $< \sim 100 \mu\text{m}$ , the peak temperature remains  $< \sim 400 \text{ K}$ . Deeper in,  $> 100 \mu\text{m}$ , the ramped wave has steepened into a shock, and the peak temperature is slightly  $> 400 \text{ K}$ . The high temperature conditions decay away over time intervals of  $\sim 100 \text{ ns}$ . The short duration of the high pressure and high temperature conditions is thought to allow the dynamically created microstructure (dislocations, stacking faults, twins, etc) to be more effectively 'frozen in' so that the residual microstructure is more closely correlated to the microstructure created dynamically. In comparison, HE loaded samples typically have high pressure conditions lasting a microsecond or longer, and the high temperature conditions last longer yet. Under the HE loaded conditions, considerable annealing, thermal recovery and recrystallisation are thought to occur, making the interpretation of the residual microstructure more problematic, especially for very high pressure loading conditions.<sup>60</sup>

Examples of our results are shown in Fig. 10 for single crystal thick Cu shocked along the [001] direction.<sup>57,61,62</sup> Samples of  $\sim 1 \text{ mm}$  thick single crystal Cu were shock compressed along the [001] direction by laser illumination with  $40$ – $320 \text{ J}$  of laser energy in a  $3.5 \text{ ns}$  pulse in a  $2.5 \text{ mm}$  diameter spot on the Omega laser. The samples were recovered from a foam filled recovery tube, sectioned and analysed by TEM. The image in Fig. 10a shows the residual microstructure resulting from an  $\sim 12 \text{ GPa}$  shock, and the image in Fig. 10b corresponds to an  $\sim 40 \text{ GPa}$  shock, along the [100] crystal orientation. The dislocation cell structure shown in Fig. 10a corresponds to the residual tangled dislocations that result from shock deformation owing to slip along the 12 dominant slip systems: four  $\{111\}$  planes and three  $\langle 110 \rangle$  slip directions within each of these planes. The residual microstructure shown in Fig. 10b is considerably different from that shown in Fig. 10a. The distinct cross hatch pattern represents traces of  $\{111\}$  planes on (001), that is, the edge on view of the four  $\{111\}$  planes cutting the (001) plane. The different hues in the criss cross pattern represents stacking fault bundles or regions of microtwins. Given that the laser induced shock direction was  $\langle 001 \rangle$ , all four  $\{111\}$  primary slip planes should be activated with equal probability, having the same Schmid factor of  $0.4082$ . The comparison between the residual dislocation cells shown in Fig. 10a and the microtwins shown in Fig. 10b suggests a twinning shock threshold between  $12$  and  $40 \text{ GPa}$ . This threshold has been estimated analytically, as described in,<sup>2</sup> giving  $P_{\text{twinning}} \approx 17 \text{ GPa}$ .

This slip twinning threshold in Cu is sensitive to other factors as well. When the orientation along which the



**a** experimental configuration for laser based and ramped loading recovery experiments; **b** typical crater results in ramp loaded single crystal Cu, showing depth of  $\sim 120 \mu\text{m}$  and diameter (at surface) of  $\sim 1.2 \text{ mm}$ ; **c** results from 2D simulations showing pressure *v.* time (curve on the left) and crater depth *v.* time (curve on the right), for experiment shown in **b**; note that crater formation is very slow process, lasting  $\sim 1 \mu\text{s}$ , compared with applied pressure pulse, which lasts only  $\sim 10 \text{ ns}$ ; **d** temperature *v.* depth into Cu sample, for loading profile shown in **c**; note that ramped compression wave steepens into shock at depth of  $\sim 120 \mu\text{m}$  into sample<sup>48,49</sup>

## 9 Recovery and crater formation

single crystal Cu is shocked is changed from [001] to [134], the slip twinning threshold increases considerably, as shown in Fig. 10c. When shocked at 40 GPa along [134], the dominant deformation mechanism is still apparently slip.<sup>57,63</sup> The suggestion is that there are fewer slip systems activated when Cu is shocked along [134]. This results in a lower probability of dislocation tangles and pinning sites, lowering the density of forest dislocations, and allowing slip (by dislocation transport along glide planes) to occur to higher shock pressures and strain rates. The deformation mechanism can also be modified by lowering the stacking fault energy, thus making twinning energetically more competitive with slip. Figure 10d shows the residual stacking faults and microtwins in Cu-6Al (wt-%), shocked along the [001] direction at  $P_{\text{shk}} \sim 12 \text{ GPa}$ . When alloyed with 6 wt-%Al, the stacking fault energy has been lowered sufficiently that stacking fault bundles and twinning are the preferred deformation mechanism at  $P_{\text{shk}} \sim 12 \text{ GPa}$  (Fig. 10d), whereas for pure Cu shocked in the same manner (Fig. 10a), slip was the dominant deformation mechanism.<sup>64</sup>

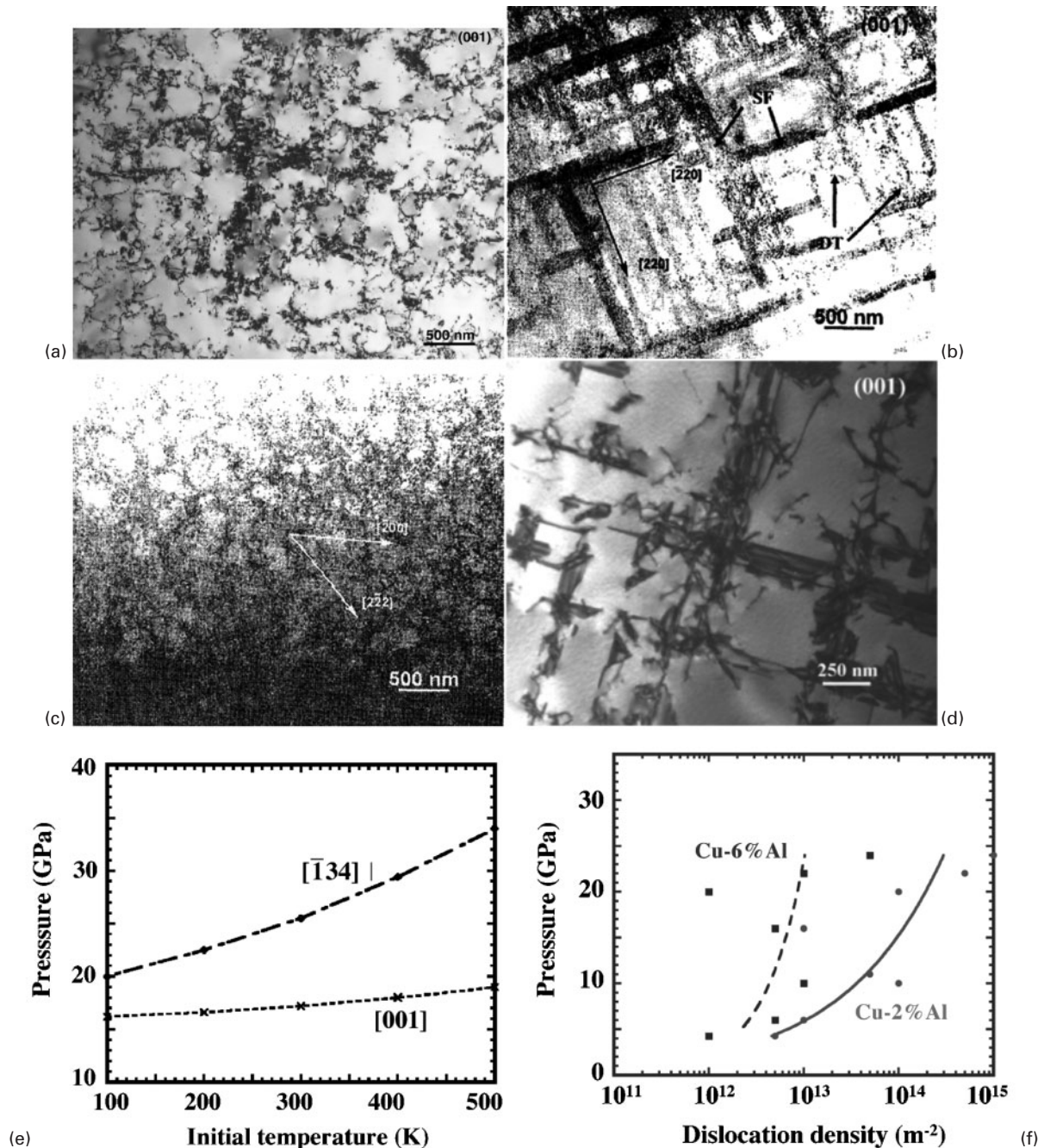
In Fig. 10e, the results of an analytic model, which has been 'calibrated' against experiment, is shown, for predicting the slip twinning threshold shock pressure for single crystal Cu shocked along the [001] or [134] directions, as a function of temperature.<sup>57</sup> As already discussed, this threshold is expected to be higher for the [134] direction, which is reflected in the analytic prediction in Fig. 10e. At high temperature, slip

becomes a more favourable deformation mechanism, which is why the curves have a positive slope.

Finally, a figure giving the residual dislocation density for Cu-2Al (wt-%) and Cu-6Al (wt-%), as a function of shock pressure is shown. Because the Cu-2Al (wt-%) has a higher slip twinning threshold, dislocation transport will be the dominant mechanism to higher shock pressures, which is why this system has the higher residual dislocation density. Nonetheless, the peak observed residual densities,  $\sim 10^{14} \text{ m}^{-2}$ , is several orders of magnitude lower than what is thought required immediately behind the shock front to relieve the shear stress, as predicted by the MD simulations shown in Fig. 8. It is thought that during decompression, owing to thermal healing the residual dislocation density is much lower, at least  $100 \times$  (maybe more) than the dynamic dislocation density required to relax the shear stress directly behind the shock front.<sup>54</sup>

## Experiments planned for NIF laser

Up until now, experiments have been performed on existing laser facilities. Pressures and strain rates achieved correspond to 10–200 GPa and  $10^6$ – $10^8 \text{ s}^{-1}$ . With the commissioning of the new NIF laser at LLNL,<sup>4</sup> an opportunity presents itself to increase the pressures of the samples in the solid state to much higher values,  $P > 10^3 \text{ GPa}$  (Ref. 5). It will be particularly interesting to see, for example, how Peierls barrier,



10 *a–d* recovery and TEM analysis of shocked samples: *a* single crystal Cu, shocked along [100] at  $P_{\text{shk}} \sim 120 \text{ kbar} = 12 \text{ GPa}$ ; *b* similar to *a* expect that  $P_{\text{shk}} \sim 400 \text{ kbar} = 40 \text{ GPa}$ ; *c* similar to *b* except that 40 GPa shock was in crystal [134] direction, instead of [100]; *d* similar to *a* expect that sample was single crystal Cu–6Al (wt-%), which has a lower stacking fault energy;<sup>2,57,63,64</sup> *e* analytic model of slip twinning threshold, for uniaxial loading along [001] and [134] directions of single crystal Cu, as function of initial temperature; *f* residual dislocation density (horizontal axis) as function of shock strength (vertical axis), and stacking fault energy (dashed v. solid curves); dashed corresponds to Cu–2%Al and solid to Cu–6%Al (Ref. 64)

shear modulus and material strength scale as pressure and strain rate are increased 100 fold above 10 GPa and  $10^5 \text{ s}^{-1}$ . At the other extreme for laser experiments, sample sizes approaching  $\sim 1 \text{ cm}$  in transverse dimension and  $\sim 1 \text{ mm}$  in thickness at pressures of a few  $\times 100 \text{ GPa}$  may be possible, using much larger laser spots and much longer ( $\sim 100 \text{ ns}$ ) pulse lengths.

In summary, the field of extreme materials science is gaining considerable interest, and new results are emerging at a fast pace. In the present paper, the progress of our working group has been reviewed in this area. All of the experiments discussed in this paper were

performed on various high energy lasers, such as the Janus, Trident, Vulcan and Omega lasers. High strain rate constitutive (strength) models were presented, showing that a key observable will be the transition from the thermal activation to phonon drag regime. A ramped shockless drive was developed to allow high pressure regimes in the solid state to be accessed. Rayleigh–Taylor hydrodynamics experiments were demonstrated to be sensitive to high (pressure, strain rate) strength models. The EXAFS diagnostic technique allows a volumetrically averaged temperature, compression and phase to be experimentally determined.

Dynamic diffraction experiments allow phase and compression to be measured, and also allow the rate of the 1D to 3D transition to be followed, which is sensitive to the dislocation density and mobility. MD simulations were shown that they were in very good agreement with EXAFS and diffraction experiments of shocked samples. Recovery and analysis of the residual microstructure were shown to allow the dominant deformation mechanism to be inferred, and in some cases 'controlled'. Dislocation densities predicted from the MD simulations are significantly higher than those observed in the residual microstructure. A very important diagnostic need for future experiments will be a dynamic, time resolved, dislocation density diagnostic.

## Acknowledgements

The present work was performed under the auspices of the US Department of Energy by the University of California, Lawrence Livermore National Laboratory under Contract No. W-7405-Eng-48, UCRL-JC-152288-ABS.

## References

- J. R. Asay: *Int. J. Impact Eng.*, 1997, **20**, 27–61.
- M. A. Meyers, F. Gregori, B. K. Kad, M. S. Schneider, D. H. Kalantar, B. A. Remington, G. Ravichandran, T. Boehly and J. S. Wark: *Acta Mater.*, 2003, **51**, 1211.
- B. A. Remington, G. Bazan, J. Belak, E. Bringa, M. Caturla, J. D. Colvin, M. J. Edwards, S. G. Glendinning, D. Ivanov, B. Kad, D. H. Kalantar, M. Kumar, B. F. Lasinski, K. T. Lorenz, J. M. McNaney, D. D. Meyerhofer, M. A. Meyers, S. M. Pollaine, D. Rowley, M. Schneider, J. S. Stölken, J. S. Wark, S. V. Weber, W. G. Wolfer, B. Yaakobi and L. Zhigilei: *Metall. Mater. Trans. A*, 2004, **35A**, 2587.
- W. J. Hogan, E. I. Moses, B. E. Warner, M. S. Sorem et al.: *Nucl. Fusion*, 2001, **41**, 567.
- B. A. Remington et al.: *Astrophys. Space Sci.*, 2005, **298**, 235.
- G. R. Johnson, J. M. Hoegfeldt, U. S. Lindholm and A. Nagy: *ASME J. Eng. Mater. Tech.*, 1983, **105**, 42.
- F. J. Zerilli and R. W. Armstrong: *J. Appl. Phys.*, 1987, **61**, 1816.
- F. J. Zerilli and R. W. Armstrong: *J. Appl. Phys.*, 1990, **68**, 1580.
- F. J. Zerilli and R. W. Armstrong: *Acta Metall. Mater.*, 1992, **40**, 1803.
- P. S. Follansbee and U. F. Kocks: *Acta Metall.*, 1988, **36**, 81.
- K. G. Hoge and A. K. Mukherjee: *J. Mat. Sci.*, 1977, **12**, 1666.
- G. Regazzoni, U. F. Kocks and P. S. Follansbee: *Acta Metall.*, 1987, **35**, 2865.
- D. J. Steinberg and C. M. Lund: *J. Appl. Phys.*, 1989, **65**, 1528.
- D. J. Steinberg, S. G. Cochran and M. W. Guinan: *J. Appl. Phys.*, 1980, **51**, 1496.
- D. L. Preston, D. L. Tonks and D. C. Wallace: *J. Appl. Phys.*, 2003, **23**, 211.
- H. J. Frost and M. F. Ashby: *J. Appl. Phys.*, 1971, **42**, 5273.
- U. F. Kocks, A. S. Argon and M. F. Ashby: 'Thermodynamics and kinetics of slip'; 1975, Oxford, Pergamon Press.
- M. A. Meyers: 'Dynamic behavior of materials'; 1994, Hoboken, NJ, John Wiley & Sons, Inc.
- P. Guyot and J. E. Dorn: *Can. J. Phys.*, 1967, **45**, 983.
- N. J. Petch: *Phil. Mag.*, 1958, **3**, 1089.
- J. Heslop and N. J. Petch: *Phil. Mag.*, 1956, **1**, 866.
- J. Heslop and N. J. Petch: *Phil. Mag.* 1958, **3**, 1128.
- W. G. Wolfer: LLNL Internal Report No. UCRL-ID-136221, 1999.
- Lorenz: in preparation for submittal to *Phys. Plasmas*, 2006.
- J. Edwards, K. T. Lorenz, B. A. Remington, S. Pollaine, J. Colvin, D. Braun, B. F. Lasinski, D. Reisman, J. McNaney, J. A. Greenough, R. Wallace, H. Louis and D. Kalantar: *Phys. Rev. Lett.*, 2004, **92**, 075002.
- T. H. Boehly, R. S. Craxton, T. H. Hinterman et al.: *Rev. Sci. Instrum.*, 1995, **66**, 930.
- J. F. Barnes, P. J. Blewett, R. G. McQueen, K. A. Meyer and D. Venable: *J. Appl. Phys.*, 1974, **45**, 727.
- J. F. Barnes, D. H. Janney, R. K. London, K. A. Meyer and D. H. Sharp: *J. Appl. Phys.*, 1980, **51**, 4678.
- P. M. Celliers, G. W. Collins, L. B. D. Silva, D. M. Gold and R. Cauble: *Appl. Phys. Lett.*, 1998, **73**, 1320.
- D. B. Hayes, C. A. Hall, J. R. Asay and M. D. Knudson: *J. Appl. Phys.*, 2004, **96**, 5520.
- D. H. Kalantar, B. A. Remington, E. A. Chandler, J. D. Colvin, D. Gold, K. Mikaelian, S. V. Weber, L. G. Wiley, J. S. Wark, A. A. Hauer and M. A. Meyers: *J. Impact Engineer.*, 1999, **23**, 409.
- D. H. Kalantar, B. A. Remington, J. D. Colvin, K. O. Mikaelian, S. V. Weber, L. G. Wiley, J. S. Wark, A. Loveridge, A. M. Allen, A. Hauer and M. A. Meyers: *Phys. Plasmas*, 2000, **7**, 1999.
- J. Colvin, M. Legrand, B. A. Remington, G. Schurtz and S. V. Weber: *J. Appl. Phys.*, 2003, **93**, 5287.
- K. T. Lorenz et al.: *Phys. Plasmas*, 2005, **12**, 056309.
- S. M. Pollaine: private communication, 2005.
- D. C. Konningsberger and R. Prins: 'X-ray absorption: principles, applications, techniques of EXAFS, SEXAFS, and XANES'; 1988, Oxford, NJ, John Wiley & Sons.
- P. A. Lee, P. H. Citrin, P. Eisenberger and B. M. Kincaid: *Rev. Mod. Phys.*, 1981, **53**, 769.
- J. Rehr and R. C. Albers: *Rev. Mod. Phys.*, 2000, **72**, 621.
- B. Yaakobi, F. J. Marshall, T. R. Boehly, R. P. J. Town and D. D. Meyerhofer: *J. Optical Soc. America B-Optical Phys.*, 2003, **20**, 238.
- B. Yaakobi, D. D. Meyerhofer, T. R. Boehly, J. J. Rehr, R. C. Albers, B. A. Remington and S. Pollaine: *Phys. Rev. Lett.*, 2004, **92**, 095504.
- B. Yaakobi, D. D. Meyerhofer, T. R. Boehly, J. J. Rehr, B. A. Remington, P. G. Allen, S. Pollaine and R. C. Albers: *Phys. Plasmas*, 2004, **11**, 2688.
- G. B. Zimmerman and W. L. Kruer: *Comments Plasma Phys. Controll. Fusion*, 1975, **2**, 51.
- B. Yaakobi et al.: *Phys. Rev. Lett.*, 2005, **95**, 075501.
- Yaakobi: *Phys. Plasmas*, 2005, **12**, 092703.
- D. H. Kalantar et al.: *Phys. Rev. Lett.*, 2005, **95**, 075502.
- J. Hawrelia: in press, proceedings of the APS-SCCM-2005.
- J. S. Wark: private communication, 2005.
- K. Kadau, T. C. Germann, P. S. Lomdahl and B. L. Holian: *Science*, 2002, **296**, 1681.
- D. H. Kalantar, J. Belak, E. Bringa, K. Budil, M. Caturla, J. Colvin, M. Kumar, K. T. Lorenz, R. E. Rudd and J. Stolken, A. M. Allen, K. Rosolankova and J. S. Wark, M. A. Meyers and M. Schneider: *Phys. Plasmas*, 2003, **10**, 1569.
- J. Hawrelia: private commun., 2005.
- A. Loveridge-Smith, A. Allen, J. Belak, T. Boehly, A. Hauer, B. Holian, D. Kalantar, G. Kyrala, R. W. Lee, P. Lomdahl, M. A. Meyers, D. Paisley, S. Pollaine, B. Remington, D. C. Swift, S. Weber and J. S. Wark: *Phys. Rev. Lett.*, 2001, **86**, (11), 2349.
- D. C. Swift et al.: *Phys. Plasmas*, 2005, **12**, 056308.
- H. E. Lorenzana: private communication, 2005.
- Bringa: Personal communication, 2005.
- K. Rosolankova et al.: in 'Shock compression of condensed matter-2003', (ed. M. D. Furnish, Y. M. Gupta and J. W. Forbes), 1195; 2004, College Park, Maryland, AIP.
- B. Sadigh: Personal communication, 2005.
- M. S. Schneider, B. K. Kad, F. Gregori, D. Kalantar, B. A. Remington and M. A. Meyers: *Metall. Mater. Trans. A*, 2004, **35A**, 2633.
- J. M. McNaney, J. Edwards, R. Becker, T. Lorenz, B. Remington: *Metall. Mater. Trans. A*, 2004, **35A**, 2625.
- J. M. McNaney, B. Torralva, J. S. Harper, K. T. Lorenz, B. A. Remington, M. S. Schneider and M. Wall: *Acta Mater.*, 2006, to be submitted.
- B. Y. Cao: *Mat. Sci. Eng. A*, 2005, **A409**, 270.
- D. H. Kalantar, A. M. Alien, F. Gregori, B. Kad, M. Kumar, K. T. Lorenz, A. Loveridge, M. A. Meyers, S. Pollaine, B. A. Remington and J. S. Wark: Proc. Conf. APS SCCM 2001, Vol. 620, 615–618; 2001, College Park, Maryland, AIP.
- M. A. Meyers, D. J. Benson, O. Vohringer, B. K. Kad, Q. Xue and H.-H. Fu: *Mat. Sci. Eng.*, 2002, **A322**, 194.
- M. S. Schneider: *Mat. Sci. Forum*, 2004, **465–466**, 27.
- M. S. Schneider: *Int. J. Impact Eng.*, 2005, **32**, 473.